The micro- and macrostructure of alumina rafts

Sindre Engzelius Gylver, Nina Helene Omdahl, Stein Rørvik, Ingrid Hansen, Andrea Nautnes, Sofie Nilssen Neverdal, Kristian Etienne Einarsrud

Abstract As alumina particles are fed to aluminium reduction cells, a frozen layer of bath is typically formed on the particle surface, due to the relatively low bath superheat. For particles in close proximity, platelets with frozen bath can be formed, resulting in agglomerates (rafts) containing solidified bath and alumina. The formation, flotation and break up of these agglomerates is determined by macroscopic properties (i.e. size, density etc.) which in turn is related to microscopic properties, i.e. how grains are interconnected. The formation of rafts delays the dissolution of alumina and thus adversely influences the conditions in the pot. In order to obtain more knowledge on the conditions for raft formation, an industrial measurement campaign was performed at Alcoa Mosjøen in which raft where collected under different operating conditions. Rafts have been characterized by micro computed

Sindre Engzelius Gylver
Norwegian University of Science and Technology (NTNU), Department of Materials Science and Engineering, Trondheim, Norway, e-mail: sindre.e.gylver@ntnu.no

Nina Helene Omdahl
Alcoa, Mosjøen, Norway, e-mail: Nina.Omdahl@alcoa.com

Stein Rørvik
SINTEF Industry, Trondheim, Norway, e-mail: Stein.Rorvik@sintef.no

Ingrid Hansen
Norwegian University of Science and Technology (NTNU), Department of Materials Science and Engineering, Trondheim, Norway, e-mail: inghanse@stud.ntnu.no

Andrea Nautnes
Norwegian University of Science and Technology (NTNU), Department of Materials Science and Engineering, Trondheim, Norway, e-mail: andrenau@stud.ntnu.no

Sofie Nilssen Neverdal
Norwegian University of Science and Technology (NTNU), Department of Materials Science and Engineering, Trondheim, Norway, e-mail: sofienn@stud.ntnu.no

Kristian Etienne Einarsrud
Norwegian University of Science and Technology (NTNU), Department of Materials Science and Engineering, Trondheim, Norway, e-mail: kristian.e.einarsrud@ntnu.no

X-ray tomography (μCT) to reveal the macroscopic properties i.e. porosity, while energy-dispersive X-ray spectroscopy (EDS) coupled to SEM and XRD has been adopted to identify the chemical composition throughout the raft. Results indicate considerable variations in macrostructure between different samples and also large differences within the same sample, depending upon the vertical position.

Key words: Alumina feeding · Agglomeration · Rafts · Characterization

1 Introduction

Feeding of alumina to industrial aluminium reduction cells is mainly performed by point feeders, in which a breaker opens a hole in the crust and introduces between 0.5 and 2 kg alumina every 1 to 3 minutes, depending upon cell size and number of feeders. A concentration between 2 and 4 weight% is required for an effective process [1]; too low concentrations ultimately lead to an anode effect, while too high concentrations limit further solubility, resulting in sludge and operational disturbances [2].

As alumina particles are fed to the cell, a frozen layer of bath will typically form on the particle surface, owing to the relatively low particle temperature compared to that of the bath, which typically is kept close to its liquidus temperature. For larger particle doses, the alumina will spread on the surface of the bath, resulting in an aggregate of particles and frozen bath. This so called raft consists of solidified bath, alumina infiltrated with bath and dry alumina [3]. During the heating of the raft, the alumina can undergo a phase transition, resulting in sintering of alumina grains [4]. The fate of the raft is partially determined by the local thermo- and hydrodynamic conditions [5], governing heat and mass transfer, but the mechanical structure, i.e. how grains are interconnected necessarily also play an important role [4].

The formation and structure of rafts and agglomerates has mainly been studied on lab scale, cf. [3], [5]-[8]. Walker et al. [6] and Kaszas et al. [7] generated compact alumina cylinders which were immersed in bath and removed for analysis after a given time, identifying a layered structure consisting of solidified bath, alumina infiltrated with bath of varying composition and finally dry alumina. The solidified bath on alumina samples is similar to that reported with respect to side ledge and crust, [9] and [10], and on anodes [11]: a dense layer was found where the bath had undergone rapid cooling, while a more porous layer was identified in regions where cooling was slower.

Industrial rafts have been described by Rolseth and Thonstad [12] and Dando et al. [13], describing features consistent with those observed in laboratory. A larger amount of pores was observed when using smelter grade alumina (SGA) than primary alumina [12], but no further investigations were made as to the origin of the pores. Pores originating from the rapid release of absorbed moisture were however recently suggested by Yang et al. [8] as an explanation to differences between measured and calculated raft densities.

Although several new important contributions have been made over the last years, several features still remain unknown, such as how the micro- and macro structure of the raft depends upon operational conditions, in particular in an industrial setting, thus motivating the current work.

2 Materials and methods

Industrial raft samples were collected from selected cells at the Alcoa Mosjøen smelter. The raft morphology is expected to depend upon the conditions under which the raft is formed, i.e. secondary alumina (SGA) properties, bath temperature and chemistry. In order to study the influence of these conditions, alumina and bath samples were collected in parallel to the rafts, as described in Gylver et al. [14]. Of the 12 rafts collected during the measurement campaign, 5 selected rafts have been analyzed further as described in table 1, together with key SGA properties and STARprobe[TM] [15] data. The rafts were selected based on intactness and relative variation in corresponding operational conditions and raft mass, measured after two months in storage.

Table 1 Overview of rafts selected for further analysis along with key operational parameters from [14]. F, BJH and MOI denote fluor concentrations (absorbed from scrubbing), porosity and moisture respectively, cf. [14] for further details, while Al_2O_3, $xsAlF_3$, T_b and T_s denote alumina concentrations, excess AlF_3, bath temperature and superheat, all of which obtained by STARprobe[TM] measurements.

Raft	F	SGA BJH ($>$3nm)	MOI (160-300)	Bath (STARprobe[TM]) Al_2O_3	$xsAlF_3$	T_b	T_s	mass m	Analysis SEM	XRD	μCT
	(wt%)	(m^2/g)	(%)	(wt%)	(wt%)	($^\circ$C)	($^\circ$C)	(g)			
1	3.0	74.8	0.8	3.7	14.5	941.8	11.1	524	Yes	Yes	Yes
2	3.0	74.8	0.8	3.7	14.5	941.8	11.1	463	No	No	Yes
5	3.0	75.3	0.7	2.2	12.8	953.5	4.5	825	Yes	Yes	No
9	8.3	71.3	0.6	2.6	9.6	966.6	6.3	597	Yes	Yes	No
10	8.3	71.3	0.6	2.6	9.6	966.6	6.3	425	No	No	Yes

The macroscopic structure has been analyzed using micro computed X-ray tomography (μCT), allowing for 3D density analysis without damaging the sample structure. The data was acquired by a Nikon XT H225 ST instrument (cone beam volume CT). A tungsten reflection target was used, with an acceleration voltage of 140 kV and a current of 220 μA. The radiation was not filtered. The imaging was done with an integration time of 1 s, amplification of 18 dB, with 3142 projections per 360°. The distance from source to sample was 306.72 mm, distance from source to detector was 1127.5 mm, resulting in a voxel size of 54.4 μm. The output of the CT scanner is a 3D volume, reconstructed with images made of sample structure.

Images were post processed and analyzed using the public domain software ImageJ [16].

The composition of the non porous part of the raft has been determined using scanning electron microscopy (SEM, 15kV) with energy dispersive spectroscopy (EDS, Jeol JCM-6000 Versatile Benchtop SEM) as well as X-ray diffraction (XRD, Rigaku MiniFlex). The Rietveld analysis was performed using PDXL2.

2.1 Sample preparation

Two small samples from rafts 1 and 10 were selected for μCT scanning, in addition to a larger piece from raft 2. The large sample was nearly intact and therefore well suited for quantitative measurements. No sample preparation was neccessary; the samples were scanned as is.

For SEM and XRD, three samples were selected from each raft, denoted as A, B and C as indicated in figure 1a, corresponding to different regions on the rafts. Owing to the porosity of the raft, samples were easily chiseled out using a scalpel. SEM samples were cast in epoxy, sawed in half using a ethanol cooled saw (Stuers Labotom 5) and polished in order to ensure a plane surface along the sample height, cf. 1b. All samples where coated with a thin layer of carbon (Quorum SC7620 Sputter Coater) and partially covered with aluminum foil in order to ensure sufficient electrical contact. For XRD, three layers where chiseled out of each sample and crushed in a mortar to an average particle size of 130 μm
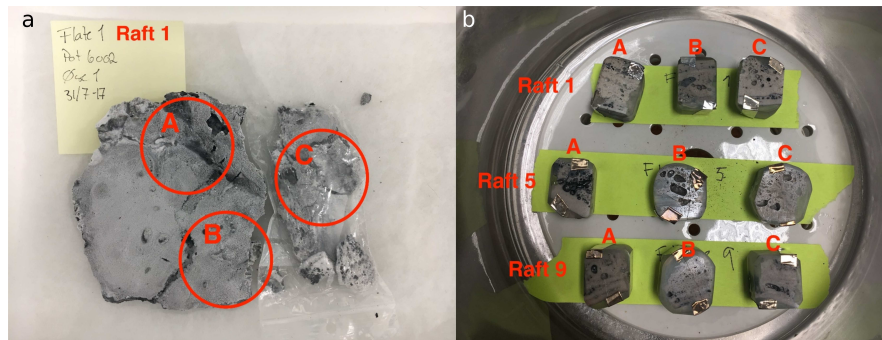
Fig. 1 Sample positioning in raft 1 (a) and prepared samples for SEM from rafts 1, 5 and 9 (b).

3 Results

For reference, sample images of raft 10 following collection (as of Gylver et al. [14]) is given in figure 2. As indicated, the intact part of the raft had a diameter of approximately 15 cm and height of 2 cm. These dimensions are typical for all the samples collected. Frames (b) and (d) reveal considerable inhomogeneities in the vertical directions as well as the expected layered horizontal structure. As indicated in figure 1b, a layered structure is present for all samples considered. Several dark regions are visible in the samples, which most likely are soot particles originating from anode dusting.
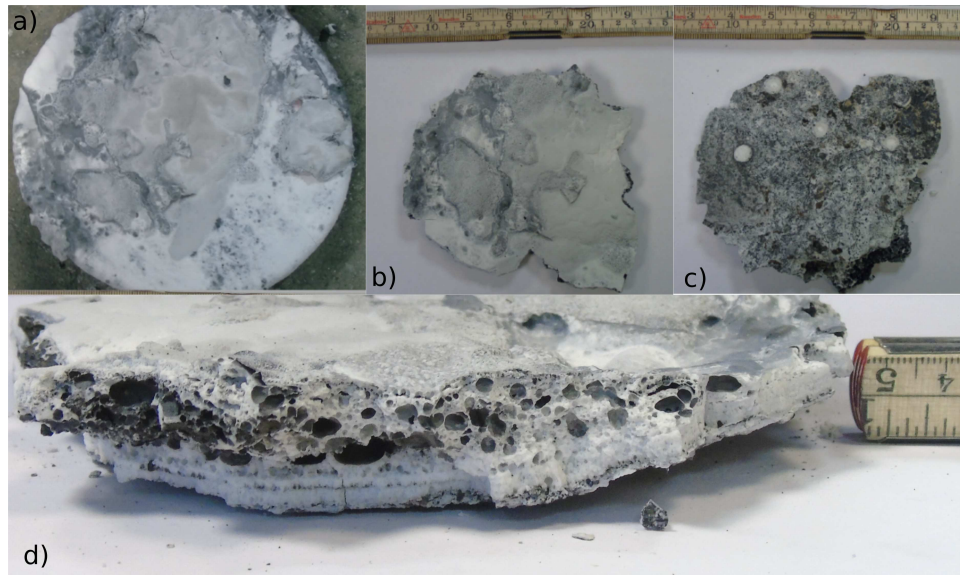
Fig. 2 Sample images of raft 10 after collection, showing a) raft on the skimming ladle, b) seen from above (after removal from ladle), c) from underneath, d) from the side, as of [14].

3.1 Computer tomography

The μCT data was calibrated to allow for quantitative measurements of the X-ray attenuation. Assuming a near constant macro-scale chemistry, i.e. approximately the same elements in the same ratios across the solidified bath regions of the sample, the density and porosity can be calculated. A solid piece of natural cryolite was added on top of the sample for calibration of the attenuation values. An assumed geometrical density of 2.95 g/cm^3 was used as a one-point calibration for the data.

Previous measurements on other materials has shown that the calculated attenuation values from the instrument are linear within $\pm 1\%$ for light element materials, so a one-point calibration is sufficient for the purpose.

Figure 3a shows a horizontal cut of the μCT data of raft 2, while 3b and 3c show the corresponding vertical cuts along the illustrated lines. The porosity increases towards the bottom region of the raft and single large pore is observed below the middle of the sample. The bottom layer is relatively dense, most likely formed from bath freezing on the ladle upon collection. The grey regions of the sample consist of carbon-enriched areas. Apparently, carbon is pushed away in the direction of electrolyte solidification. The rectangular solid white piece above the sample seen in the XZ (figure 3b) cut is the cryolite calibration piece; removed from the dataset in the analysis.

The density and macro-porosity values were calculated as a function of vertical position as shown in figure 4. The term macro-porosity means porosity seen in the μCT scans, well above the resolution of 54μm. The porosity is reported as a percentage of pores relative to the entire horizontal cross-sectional area of the sample (including the pores). The discontinuities of the curves are due to variations in which individual pores are found to be entirely inside or partially outside the sample; the latter is excluded. The calculated total density value for the entire sample is 1.76 g/cm^3 and the total porosity value is 12.72%. The calculated density is thus well below the assumed density of 2.05 g/cm^3 for the molten bath, explaining why this sample will float. It is also evident from Figure 4 that only the lowest zone (frozen bath on the ladle) is higher than the density of molten bath.

The porosity was found to be 18.15% and 22.05% for the samples from rafts 1 and 10, distributed in a non-monotonous manner corresponding to that seen in figure 4. As these were smaller samples, the values are less representative than those obtained from the full scan of raft 2. Nevertheless, the values give an impression of the variation in porosity.
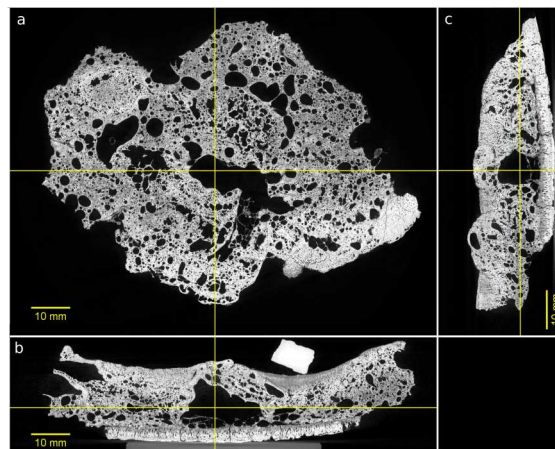

Fig. 3 Sample images from μCT scanning of raft 2 showing horizontal (XY) (a), vertical (xz) (b) and vertical (yz) (c) cuts of the sample.

Fig. 4 Distribution of density (blue dashed line) and porosity (orange dotted line) as a function of distance from raft bottom for raft 2.
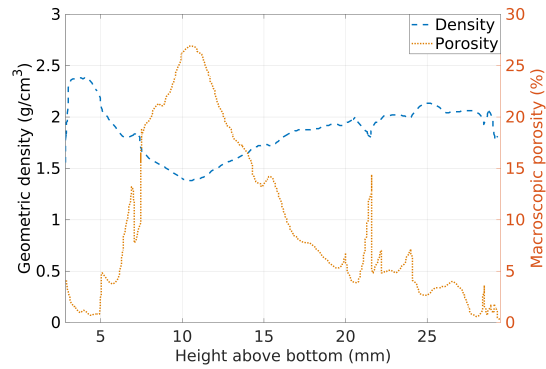
3.2 SEM

Qualitative chemical analysis has been performed on each of the rafts considered using SEM-EDS. For each of the samples (A-C, cf, figure 3.2a), EDS mapping and point analysis was performed in order to determine the chemical composition in nine different heights (A-G), relative to the raft bottom. In each height, the mapping was performed in three separate regions. Sample images from the top and bottom regions of raft 1, sample B are shown in figure 5.
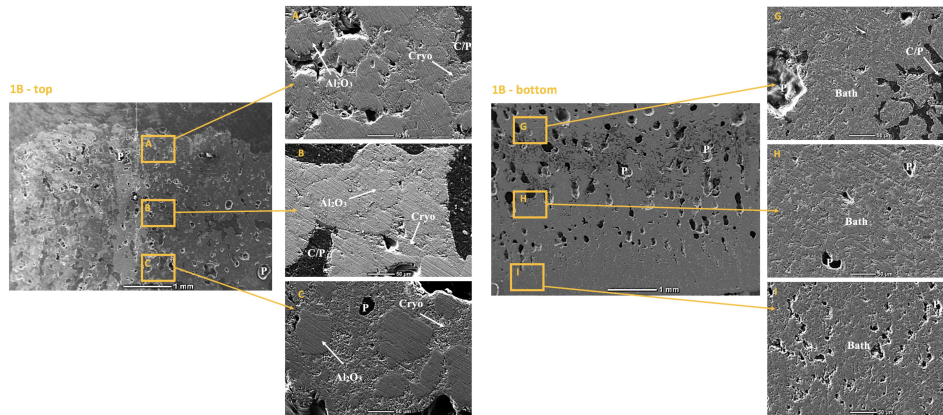

Fig. 5 SEM images from top and bottom regions of raft 1B. Al_2O_3 denotes undissolved alumina grains, Cryo/Bath denotes bath and C/P denotes carbon rich pores.

Three different morphologies of interest where identified; relatively smooth grains, rich in Al and O assumed to be (undissolved) alumina particles, a rougher flaky structure rich in Na, Al and F with some Ca, O and C, assumed to be bath with

dissolved alumina and finally dark pitted regions - pores - found to be rich in C. The carbon detected in the pores is most likely a consequence of the carbon coating applied to the samples, but as seen from figure 2d, the pores appear considerably darker than the raft itself, suggesting that there is some carbon present also before coating. Unfortunately, it is however not possible to discern the different carbon sources with the current analysis.

The mean composition (wt%) from rafts 1A, 1B and 5B as a function of height for the elements considered is shown in figures 6a and 6c, respectively, where the error bars represent the (sample) standard deviation at the given height.
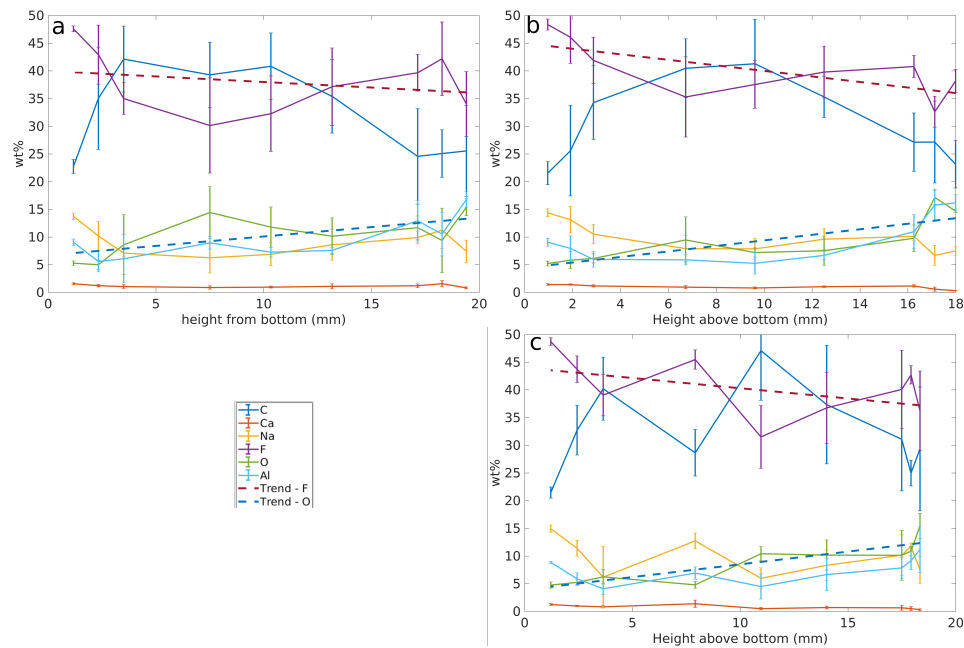
Fig. 6 Distribution of elements as function of vertical position in raft sample 1A (a), 1B (b) and 5B (c). The error bar corresponds to $\pm\sigma$ at the given height. Trend lines are shown for fluorine (red dashed line) and oxygen (blue dashed line).

The distribution of elements shown in figure 6 indicates that although there are some differences between the profiles of the different samples - these variations are comparable to the variation found at a given height for a single sample. For each of the samples considered, Na, F and Ca are found to decline with increasing distance from the raft bottom, while O and Al are found to increase - as indicated with the trend lines shown in figure 6. Fluorine is here assumed to be representative of the bath phase, while oxygen is assumed to be representative of alumina.

The mean distribution of F (bath), O (alumina) and C (pores/soot) in top (14-20 mm), middle (4-14 mm) and bottom (0-4 mm) parts of each raft is shown in table 2, with one standard deviation as a measure of the variation.
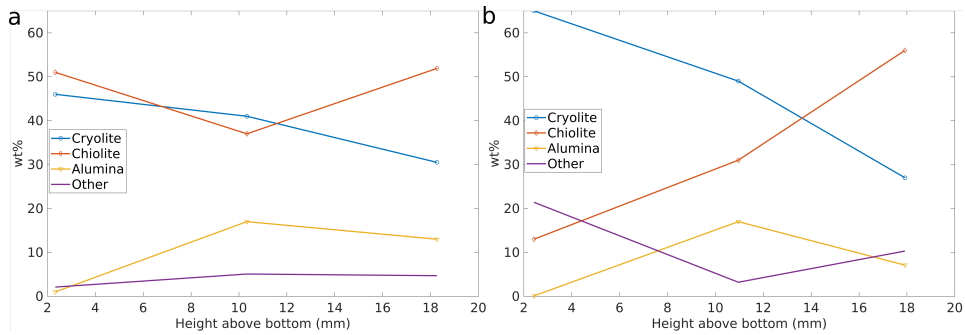
Table 2 Overview of mean distribution of key elements in top, middle and bottom layers as of EDS analysis. The variation is indicated as $\pm\sigma$.

Raft	Top			Middle			Bottom		
	F	O	C	F	O	C	F	O	C
(#)	(wt%)	(wt%)	(wt%)	(wt%)	(wt%)	(wt%)	(wt%)	(wt%)	(wt%)
1	38 ± 5	12 ± 4	25 ± 6	36 ± 6	10 ± 4	36 ± 7	44 ± 5	6 ± 2	30 ± 9
5	40 ± 6	11 ± 4	30 ± 9	32 ± 10	12 ± 5	44 ± 13	43 ± 6	5 ± 1	31 ± 10
9	32 ± 12	13 ± 8	35 ± 12	44 ± 6	6 ± 3	30 ± 9	36 ± 11	5 ± 1	36 ± 7

3.3 XRD

For each of the samples considered for SEM, XRD was performed on three layers corresponding to the top, middle and bottom part of the sample, resulting in a single data point for each layer. Phases were separated into alumina, cryolite, chiolite and other - signifying all other (secondary) phases. The distribution of these phases for samples 1A and 5B is shown in figure 7 as a function of the mean height above the raft bottom at which the layer was removed from.

Fig. 7 Distribution of phases as function of vertical position in raft sample 1A (a) and 5B (b).

Corresponding to the results presented in table 2, a summary of the XRD data for each of the rafts considered is given in table 3, where average values are calculated based on each of the three samples (A, B, C; cf. figure 1) considered.

Table 3 Overview of mean distribution of key phases - cryolite (Cry), chiolite (Chi), alumina (Alu) and other - in top, middle and bottom layers as of XRD analysis. The variation is indicated as $\pm\sigma$.

	Top				Middle				Bottom			
Raft	Cry	Chi	Alu	Other	Cry	Chi	Alu	Other	Cry	Chi	Alu	Other
(#)	(wt%)	(wt%)	(wt%)	(wt%)	(wt%)	(wt%)	(wt%)	(wt%)	(wt%)	(wt%)	(wt%)	(wt%)
1	25±8	62±10	7±6	7±4	42±5	27±23	22±12	10±7	49±3	39±16	4±5	8±9
5	35±8	48±7	11±6	6±5	48±1	32±1	15±3	6±5	61±7	27±13	1±2	11±9
9	45±9	40±7	3±2	11±4	60±9	31±2	4±6	5±1	69±7	22±4	1±1	8±6

4 Discussion and concluding remarks

Industrial rafts have been collected and micro- and macroscopic properties have been determined.

CT and SEM images reveal a considerable variation in porosity - from 1% close to the raft bottom and up to 30% in the middle sections. The presence of pores reduces the (geometric) density of the raft to values lower than that of the bath, thus contributing to buoyancy. The underlying mechanisms which generate the pores is not investigated in detail in the current scope, but the evolution of volatiles such as water vapour and HF gases are likely candidates, resulting in gaseous bubbles trapped in the bath as it freezes.

The relatively dense region towards the bottom of the samples, visible in figures 1 and 3 is most likely due to the rapid freezing of bath on the ladle - consistent in structure and composition to that observed by Liu et al [10] in cold finger experiments. Correspondingly, a rapidly frozen layer is expected to form on the alumina raft as well - possibly explaining the presence of multiple layers, here observed as a non-monotonous change in properties.

SEM-EDS analyses indicate that fluorine, calcium and sodium levels decline towards the upper parts of the rafts, while amounts of aluminium and oxygen are found to increase, believed to indicate that bath infiltrates the alumina powder also in an industrial setting - as indicated in lab scale experiments previously (cf. [3]). XRD results, cf. figure 7 indicate the dominating phase close to the bottom of the raft is cryolite, while the composition is more AlF_3 rich (chiolite) towards the upper part of the raft - consistent with the models for infiltration proposed by Walker [6] and Østbø [4] in which the raft is formed by subsequent freezing, remelting and infiltration steps. XRD results indicate that the amount of alumina is largest in the middle section of the raft, rather than the upper. Although a larger sample size is needed to confirm this, one possible explanation could be due to splashing of bath on the top of the raft, as described in [14].

Regarding bath properties (cf. table 1), results indicate, unsurprisingly, that the bath composition is transferred to the raft. The bath surrounding Raft 1 had the highest levels of AlF_3 - observed as elevated levels of chiolite in the XRD data.

SGA properties are found to vary between the different rafts considered. In particular, MOI and F are related gas evolution. Considering rafts 1 and 2 in particular, the (relatively) high values of MOI may lead to increased HF formation (cf. [13]), possibly explaining the large pores observed in these rafts.

Results indicate similar large scale, porous structures for all of the rafts considered, i.e. multiple layers gradually depleted of bath towards the upper regions. There is a considerable variation in different samples from the same raft, comparable to the variation found when comparing different rafts.

References

1. Grjotheim, K., Kvande, H.: Introduction to Aluminium Electrolysis, 2nd Edition. Aluminium Verlag, Dusseldorf (1993)
2. Lavoie, P., Taylor, M. P., Metson, J.B.: A Review of Alumina Feeding and Dissolution Factors in Aluminium Reduction Cells. Met. Mat. Trans. B **47**, pp. 2690-2696 (2016)
3. Kaszas, C., Kiss, L., Poncsak, S., Guerard, S., Bilodeau, J.F.: Spreading of Alumina and Raft Formation on the Surface of Cryolitic Bath. In: Ratvik, A.P. (Ed.) Light Metals 2017, pp. 473-478, Springer, Cham (2017)
4. Østbø, N.P.: Evolution of Alpha Phase Alumina in Agglomerates upon Addition to Cryolitic Melts. Ph.D. Thesis 50, Norwegian University of Science and Technology - NTNU (2002)
5. Walker, D.I.: Alumina in aluminium smelting and its behaviour after addition to cryolite-based electrolytes. Ph.D. Thesis, University of Toronto (1993)
6. Walker, D.I., Utigard, T., Taylor M.P.: Alumina agglomerates in aluminium smelters. In: Evans, J.W. (Ed.) Light Metals 1995, pp. 425-434, TMS, Warrendale (1995)
7. Kaszas, C., Kiss, L., Poncsak, S., Bilodeau, J.F., Guerard, S.: Floatation and Infiltration of Artificial Rafts on the Surface of Molten Cryolite. In: Proceedings of the 34th International Conference and Exhibition of ICSOBA, AL-27, Quebec (2016)
8. Yang, Y., Gao, B., Wang, Z., Shi, Z., Hu, X.: The Formation and Dissolution of Crust Upon Alumina Addition into Cryolite Electrolyte. JOM **67**, pp. 583-588 (2015)
9. Poncsak, S., Kiss, L., Raymond, V.D., Kaszas, C., Gurard, S., Bilodeau, J.F.: Impact of the Heat Flux on Solidification of Cryolite Based Bath. In: Williams, E. (ed) Light Metals 2016, pp. 359-364. Wiley, Hoboken (2016)
10. Liu, J., Fallah-Mehrjardi, A., Shishin, D., Jak, E., Dorreen, M., Taylor, M.P.: Investigation of the Influence of Heat Balance Shifts on the Freeze Microstructure and Composition in Aluminum Smelting Bath System: Cryolite-CaF_2-AlF_3-Al_2O_3. Met. Mat. Trans B, **48**, pp. 3185-3195 (2017)
11. Picard, D., Tessier, J., Gauvin, G., Ziegler, D., Alamdari, H., Fafard, M.: Investigation of the Frozen Bath Layer under Cold Anodes. Metals, **7**, pp. 374-383 (2017)
12. Rolseth, S., Thonstad, J.: Agglomeration and dissolution of alumina in cryolite baths. In: Sahoo, M., and Pinfold, P. (Ed.): Extraction, Refining and Fabrication of Light Metals. pp. 177-190. Pergamon, Amsterdam (1991)
13. Dando, N., Wang, X., Sorensen, J., and Xu, W.:Impact of thermal pretreatment on alumina dissolution rate and HF evolution. In: Johnson, J.A. (ed.) Light Metals 2010, pp. 541-546, Wiley, Hoboken (2010)

14. Gylver, S.E., Omdahl, N.H., Prytz, A.K., Lossius, L.P., Meyer A.J., Einarsrud, K.E.: Alumina feeding and raft formation: Raft collection and process parameters. In: Chesonis, C. (ed.) Light Metals 2019, Springer, Cham, (2019)
15. Wang, X., Hosler, B., Tarcy, G.: Alcoa STARprobe^{TM}. In: Lindsay, S. (ed.) Light Metals 2011, pp. 483-489, Wiley, Hoboken (2011)
16. Rasband, W.S.: ImageJ. U. S. National Institutes of Health, Bethesda, Maryland, USA, http://imagej.nih.gov/ij/, (1997-2016)